Electron ionization dynamics of N_2 and O_2 molecules: Velocity-map imaging

James N. Bull,* Jason W. L. Lee, and Claire Vallance†

Chemistry Research Laboratory, Department of Chemistry, University of Oxford, 12 Mansfield Road, Oxford OX1 3TA, United Kingdom

(Received 6 November 2014; revised manuscript received 26 December 2014; published 9 February 2015)

This paper reports a crossed-beam velocity-map imaging study into the electron ionization dynamics of jet-cooled N_2 and O_2 molecules at electron collision energies from 35 to 100 eV. The use of velocity-map imaging detection provides insight into the detailed ionization dynamics through the dimension of the product ion kinetic energy associated with impulsive dissociation. In particular, "mesoscopic" cross sections corresponding to ionization from manifolds of energetically close states converging to the same dissociation asymptote are reported for a number of single-ionization channels. In addition, a range of double-ionization cross sections have been characterized, including those yielding $X_2{}^{2+}$ dications. These are found to be in excellent agreement with other cross sections determined in coincidence measurements. This agreement supports a meaningful and accurate determination of the single-ionization channels.

DOI: 10.1103/PhysRevA.91.022704 PACS number(s): 34.80.Ht, 06.30.Gv, 34.80.Gs

I. INTRODUCTION

Molecular nitrogen N_2 and oxygen O_2 are two benchmark molecules within the field of ion physics due to their abundance and importance in planetary atmospheres and interstellar chemistry, as well as in laboratory plasmas [1–6]. For example, N_2 and O_2 constitute some 78% and 21% of Earth's atmosphere by volume, respectively, and N_2 is the major component of the atmospheres of Titan (94%) and Triton (99.99%), the largest moons of Saturn and Neptune, respectively. Within the upper reaches of planetary atmospheres, energetic electrons are produced either through high-energy photoionization or via the capture of solar wind electrons by a planetary magnetosphere. Such electrons may induce a variety of ionization processes, with the resulting ions playing an important role in the chemistry of the upper atmosphere [2,4,7,8]. As a specific example, Titan's upper atmosphere consists mainly of N_2 and CH_4 species that through ion-molecule reactions are the precursors of complex organic tholins present in the lower atmosphere; the present conditions on Titan are thought to be similar to those on primordial Earth [7,9–14]. Electron ionization processes are similarly thought to play a role in the upper atmosphere of Triton [15–17]. In these astrophysical examples and indeed also for laboratory plasmas, modeling of the ion-molecule processes requires knowledge of the ionization process in which the ionic species are formed, including ionization probabilities or cross sections and ion internal state distributions.

Electron ionization, formerly widely known as electron-impact ionization, is one of the most fundamental processes in collision physics [1]. The collision between a free electron, $e^-(E_i)$, with initial kinetic energy E_i (35–100 eV in this work), and a gas-phase molecule, AB, may induce vertical ionization:

$$e^-(E_i) + AB \rightarrow AB^+ + e^-(E_f) + e^-(E_e),$$

where $e^-(E_f)$ is the scattered electron, with kinetic energy E_f, and $e^-(E_e)$ is the ejected or "ionization" electron, with kinetic energy E_e. The energy available to the products, equal to the energy transferred in the collision, $\Delta E = E_f - E_i$, less the vertical ionization potential of the ejection electron, is initially apportioned in some way between E_e and internal excitation of the nascent parent cation, AB^+. The distribution of ΔE across many collisions or the partitioning of ΔE between the electron and ion is not revealed in most experiments. The neutral and ionic electronic states accessible in an electron-molecule collision are not strictly governed by optical dipole selection rules, and, in principle, a large number of nascent states of energies up to the collision energy can be accessed. In practice, electron ionization is usually an inefficient collision process, in that only a small portion of the electron kinetic energy is transferred in the collision. Within the commonly used framework of Bethe theory [18], the majority of ionizing collisions are of glancing nature, with large impact parameters [19]. Because N_2 and O_2 molecules have only one vibrational degree of freedom along the bond from which the electron is ionized, dissociation from unbound ionized states populated in the electron-molecule collision is (usually) rapid, and the kinetic-energy distribution of the fragments strongly reflects the dissociative state and its Franck-Condon overlap with the ground state. In more complex molecules, the number of valence electrons increases and consequently the number of accessible ionized states increases. When coupled with the distribution in the amount of energy transferred from the incoming electron to the molecule, the process yields canonical ensembles of parent ion (vibronic) microstates. In contrast to electron ionization, photoionization deposits a known quantity of energy into the molecule, initially yielding a parent ion microcanonical ensemble of a well-defined total (electronic) energy. The known total energy makes interpretation of the fragment distributions in terms of energy partitioning and statistical vs impulsive models of the dissociation dynamics simpler than in the case of electron ionization. However, as will be demonstrated, the ion velocity distributions recorded in an electron ionization experiment are still information rich.

The present study details an electron-molecule crossed-beam imaging study into the ionization dynamics of N_2 and O_2 over the electron energy range from 35 to 100 eV. By measuring the ion fragment kinetic energy (termed kinetic-energy release or KER, herein) associated with ion production

*Present address: Department of Chemistry, Durham University, South Road, Durham DH1 3LE, United Kingdom; james.bull@eigenket.org

†Corresponding author: claire.vallance@chem.ox.ac.uk

as a function of incident electron energy, and applying a simple diatomic dissociation model, "mesoscopic" cross sections, which correspond to groups (or "manifolds") of energetically close states dissociating to the same asymptote, have been determined. These mesoscopic cross sections have not been previously characterized in the case of single ionization. In addition, the procedure also produces double-ionization cross sections, for both X^+, X^+ and $X_2{}^{2+}$ channels.

A key advantage in the present study is the use of velocity-map imaging (VMI) in the detection step [20–23]. Compared with conventional rotatable detectors, VMI provides improved data acquisition rates, and true "velocity-mapped" angular distribution without any blurring caused by the finite size of the interaction region. Despite these considerable advantages, the application of VMI detection to ionization processes other than photoionization has been limited [20,24–29].

II. EXPERIMENTAL METHODS

The electron-molecule crossed-beam VMI instrument used in the present study has been described previously [20]. During an experiment, 180 μs pulses of N_2 or O_2 gas (BOC > 99.9% purity) are admitted to the instrument via a Parker-Hannifin Corp. Series 9 pulsed solenoid valve. The gas pulses are crossed at right angles with a pulsed electron beam of ~30 ns pulse duration, with a selected kinetic energy between 35 and 100 eV and FWHM energy resolution of ~0.25 eV, generated from a modified PSP Vacuum Technology ELS100 LaB_6 single-crystal electron source. The electron beam diameter is ~1 mm at the interaction region. The velocity-mapping ion optics consist of a conventional three-electrode arrangement (repeller, extractor, and ground) [22,23], encased within a mu-metal shield to eliminate stray magnetic fields from the interaction region. The velocity-mapping lens pulsing sequence is electrically controlled via a pair of Behlke HTS-101 fast transistor switches. All three velocity-mapping electrodes are grounded while the electron pulse traverses the interaction region. As soon as the electron pulse has cleared the lens assembly, the repeller and extractor electrodes are pulsed to their velocity-mapping potentials with a rise time of around 8 ns. Repeller potentials of 7 and 5 kV are used for N_2 and O_2, respectively, combined with one of two flight tubes of length 240 and 480 mm, respectively. The shorter flight tube allows collection of the complete KER distribution, while the latter allows acquisition of "zoomed in," higher-resolution KER distributions in the low-energy region near the center of the image. After traversing the flight tube, the ions are incident on a position-sensitive ion imaging detector consisting of two 40 mm chevron-mounted multichannel plates (MCPs) coupled to a P47 phosphor screen. Images produced on the phosphor are captured by a Photonic Science MiniFDI intensified CCD camera, time gated to the arrival time of the ion of interest, and the total (time-dependent) signal at the phosphor is monitored by a Hamamatsu H10721-01 photomultiplier, allowing the complete time-of-flight spectrum to be recorded in tandem with the image of interest. The repetition rate of the experiment was limited to ~15 Hz by the acquisition speed of the CCD camera.

There have been several instrumental improvements since the publication of our earlier communication [20]. The electron pulse width has been reduced by around 10 ns following improvements to the electron gun pulse driver, the Behlke switch resistance-capacitance circuits have been retuned in order to optimize the performance of the extractor and repeller pulsing, and the skimmer assembly has been further optimized to achieve a higher-quality supersonic expansion. The velocity-mapping resolution is characterized to be ~3.5%, which is a small improvement over the ~5% reported in our initial communication.

Electron ionization of N_2 and O_2 produces three dominant ion species in each case: the parent ion $X_2{}^+(m/z = 28 \text{ or } 32)$, the fragment ion X^+ $(m/z = 14 \text{ or } 16)$, and the doubly charged parent ion $X_2{}^{2+}(m/z = 14 \text{ or } 16)$, where X denotes N or O, respectively. Images for ions with $m/z = 14$ and 16 were accumulated over 500 000 acquisition cycles at selected incident electron energies in the range from 65 to 100 eV. Images acquired for electron energies between 40 to 60 eV were accumulated over two- or threefold this number of counts in order to achieve a comparable signal-to-noise ratio. Signal levels are lower at lower electron energies due both to the reduced emissivity of the source within the electron gun and the reduction in the electron ionization cross section at these energies.

Each image was processed on-the-fly using thresholding, centroiding, and event-counting algorithms [30], and was background corrected postacquisition by subtracting an image recorded under conditions in which the electron pulse had cleared the interaction region shortly before arrival of the molecular beam. The background image contains all contributions from ionized background gas in the vacuum system, but does not contain contributions from the molecular beam. Because the $N_2{}^{2+}$ partial ionization cross section is relatively large, it was necessary to accumulate event-counted images at sufficiently low count rates to minimize loss of the dication signal due to two or more events either illuminating a single camera pixel (cf., centroiding) or saturating the microchannel plates near the center of the image within a given time-of-flight cycle. These effects were studied systematically prior to data collection in order to ensure that this condition was satisfied.

The image acquisition software records the number of ions impinging on the detector, i.e., a counting cross section, such that $N_2{}^{2+}$ or $O_2{}^{2+}$ is "imaged" as one count. The detector assembly and camera are operated under linear gain conditions; Ar^{2+}/Ar^+ and Ne^{2+}/Ne^+ ratios were routinely recorded and ensured to match those from well-reviewed measurements [31,32]. Of note in the discussion below, a gross cross section records $X_2{}^{2+}$ (or a correlated ion pair, N^+, N^+) as two counts.

A. Fragment ion angular distributions

One key feature of VMI detection is the ability to characterize any angular anisotropy in the measured fragment ion distributions. As first detailed by Dunn and co-workers [33,34] and further discussed in a number of publications including Zare [35] and Misakian *et al.* [36], these anisotropies arise from a combination of the symmetry of the electron-molecule ionization interaction and momentum transfer during the electron ionization collision [37–39]. In many cases, the excitation and ionization efficiency depends on the relative orientation of the incoming electron beam and the molecule

[40,41], in much the same way as photoexcitation depends on a favorable overlap between the polarization of the exciting radiation and the transition dipole associated with the transition of interest. If the resulting internally excited ion dissociates on a time scale that is fast compared with the time scale of molecular rotation, the velocities of the dissociation products will be aligned predominantly along the direction of the vibrational motion associated with bond cleavage. The second possible source of anisotropy is momentum transfer from the electron beam to the molecular ion [36], which imparts an additional net forward asymmetry to the fragment ion angular distribution. All images recorded in the present study exhibit only momentum transfer anisotropy in the fragment ion velocity-map images.

B. Data fitting procedure

The velocity-map images represent two-dimensional projections of the full three-dimensional (3D) ion fragmentation distributions along the time-of-flight axis. When the ion fragmentation distribution has an axis of cylindrical symmetry, as in the present case, the speed distribution of the ions can be determined by performing an inverse Abel transform on the image, which returns the central slice through the 3D distribution, and integrating this slice over the angular coordinate [24]. The speed distribution may then be converted into a kinetic-energy release distribution via a simple coordinate transformation. While this is a widely adopted procedure, even the best algorithms for performing the inverse Abel transform tend to introduce noise into the data. In the present work, this complication was avoided by fitting the radial distributions obtained from the crushed images directly. The kinetic-energy release distribution was expanded as a sum of Gaussian-like functions (this choice of basis function is discussed further below), and a forward-convolution procedure was used to generate the corresponding radial distributions for the crushed images, which could be fitted directly to the corresponding distributions extracted from the experimental data. As a check, the KER distributions returned from the fitting and forward-convolution procedure were compared with those obtained using the popular polar onion peeling (POP) algorithm [42].

The images acquired for all electron energies were fitted simultaneously by requiring the mean kinetic energy and full-width at half maximum of the basis functions to remain constant, with only the relative intensity of each basis function allowed to vary between images acquired at different electron energies. Systematic mapping of the parameter hypersurface ensured that the final fits represented a global minimum. The fitting procedure employed the minimum number of basis functions that were able to satisfy the criteria of (i) providing good overall fits to the data and accounting for all observed spectral features, (ii) yielding similar fits for individual data sets whether they were fitted separately or as part of a global fit, (iii) producing extracted cross sections that exhibit reasonable electron energy thresholds and a smooth electron energy dependence, and (iv) returning results in agreement with previously published data, where available. Basis sets consisting of ten and 11 functions were used to fit the data for $m/z = 14$ and 16, respectively.

Within the fitting procedure, each Gaussian-like basis function represents the contribution (mesoscopic cross sections) from a given dissociation asymptote to the overall fragment ion KER distribution. It is assumed that Gaussian-like basis functions provide a reasonable description of such contributions for several reasons: (i) the reflection approximation [43] tends to be valid for diatomics, since there is only one dissociation coordinate, (ii) all studies to date have failed to observe significant fine structure in the measured KER distributions, and (iii) principal component analysis performed on each data series confirmed both that the contributions from each component eigenvector were closely Gaussian-like in functional form, and that the number of basis functions determined in the simultaneous fitting procedure was approximately correct. In addition, the principal component analysis revealed which basis functions were approximately parallel (but sufficiently resolved in the KER domain). The contribution from doubly charged parent ions was assumed to take the same functional form as that for singly charged parent ions, simply reflecting the kinetic-energy distribution of the neutral parent molecules in the molecular beam.

Finally, for a homonuclear diatomic, the measured fragment ion energy or KER in this study is equal to half of the total kinetic-energy release in the dissociation.

All ionization cross sections determined in this work are numerically tabulated in the Supplemental Material, with uncertainties given at the 95% confidence level [44].

III. RESULTS AND DISCUSSION

A. Nitrogen

Radial distributions of the measured velocity-map images for $m/z = 14$ (transformed into dimensions of KER), together with the forward-convoluted contribution from each basis function are shown in Fig. 1 for three selected electron energies. Although KER distributions have been reported in

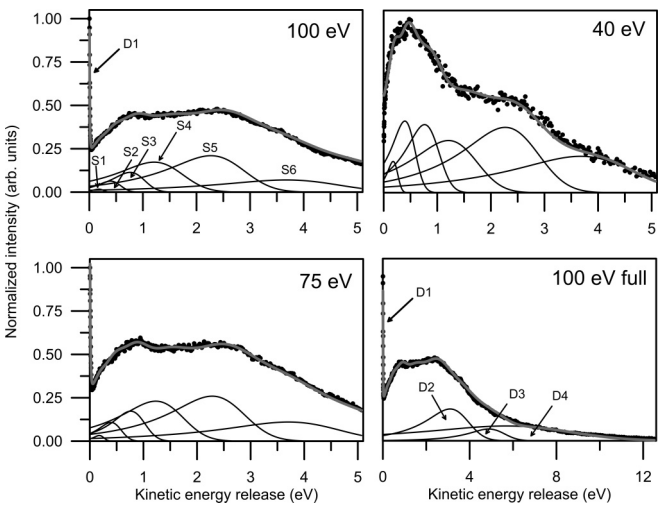

FIG. 1. Radial distributions and final forward-convoluted fits for the images of N^+ and N_2^{2+} formed in the electron ionization of N_2. Note that intensity is multiplied by the image radius in order to better illustrate the high-KER features. S1–S6 and D1–D4 are defined in the text.

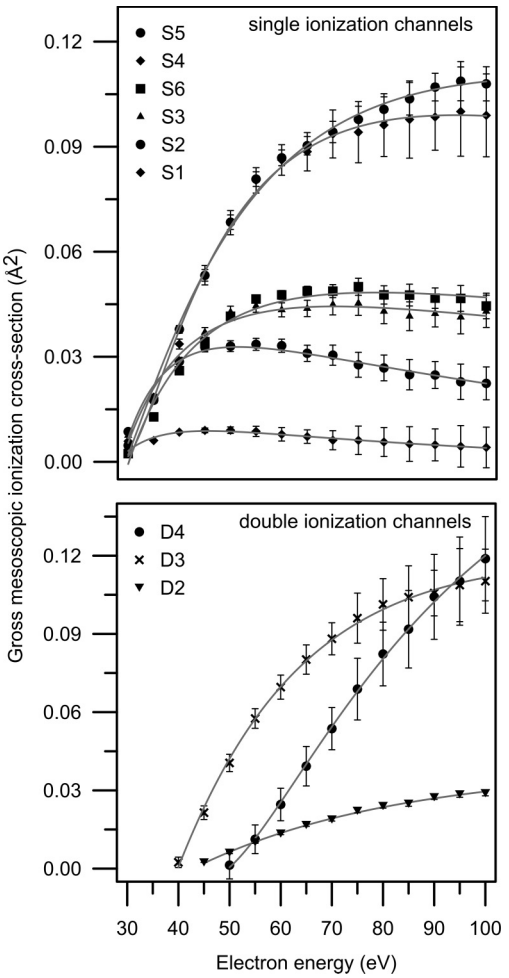

FIG. 2. Mesoscopic ionization cross sections for the nine fragment kinetic-energy release manifolds of N^+.

a number of early studies, namely, those of Van Brunt and Kieffer [45], Locht *et al.* [46], Deleanu and Stockdale [47], and Köllmann [48], the large errors (30–50% in magnitude) and low KER resolution (between ∼0.25 and 1.0 eV) did not permit any reliable mesoscopic cross-section determination. In accord with an earlier study [49], the present data and model indicate that there are five predominant and distinct dissociation asymptotes resulting from single ionization: $N^+(^3P) + N(^4S)$; $N^+(^3P) + N(^2D)$; $N^+(^3P) + N(^2P)$; $N^+(^1D) + N(^2D)$; and $N^+(^1D) + N(^2P)$. In addition, the earlier rotatable detector studies all indicated relatively isotropic scattering distributions for incident electron energies of 40 eV or greater, which is consistent with the present study [39,45,47,50].

The mesoscopic cross sections as a function of electron energy are shown in Fig. 2. These cross sections have been normalized such that the total area for each KER distribution is equal to the partial ionization cross section (PICS) previously determined with the same instrument [20]. The ten basis functions required to achieve a globally acceptable fit have been assigned to six single-ionization manifolds, denoted S1 to S5, and four double-ionization manifolds, denoted D1 to D4. The mean KERs for the single-ionization contributions are S1 = 0.25(13), S2 = 0.55(1), S3 = 0.98(1), S4 = 1.64(4), S5 = 2.77(3), and S6 = 4.46(8) eV.

Manifold S1 is assigned to autoionization of Rydberg states. There have been a number of studies reporting KER and angular distributions of Rydberg and high-Rydberg nitrogen atoms following electron impact of N_2 [51–54]. These studies all returned similar KER distributions to earlier electron ionization distributions for N^+, although with an additional small feature centered around 0.3 eV assigned to the manifold of states converging to the $N^+(^3P) + N(^4S)$ asymptote.

Manifolds S2 and S3 arise predominantly from the well-known $C\,^2\Sigma_u^+ \leftarrow X\,^1\Sigma_g^+$ ionizing transition. The C state is bound in the Franck-Condon region and correlates with the $N^+(^3P) + N(^2D)$ or S2 dissociation asymptote. Vibrational states with $v \geqslant 3$ are known to predissociate, and have been the subject of a number of experimental and theoretical studies [55–58, and references therein]. At $v = 3$, the predissociation rate is slow and competitive with fluorescence; the rate increases linearly with increasing v. There are two different predissociation models postulated, known as the accidental and direct models, the latter of which is now more generally accepted [55]. Assuming the direct predissociation model, the above vibrational window of the $C\,^2\Sigma_u^+$ state predissociates via the $B\,^2\Sigma_u^+$ continuum state, correlating with the $N^+(^3P) + N(^4S)$ or S3 dissociation asymptote. The electron ionization experiments of Locht *et al.* [46] using the retarding potential technique similarly observed vibrational structure comparable with the recent photoionization experiments noted above. Van Brunt and Kieffer [45,59] tentatively observed forward-backward peaking angular distributions for N^+ formed within the S2 and S3 manifolds near threshold, in accord with Dunn's rules [33] for a formally allowed $\Sigma_u^+ \leftarrow \Sigma_g^+$ parallel transition.

Manifold S4 is thought to correlate with the $N^+(^3P) + N(^2P)$ dissociation asymptote, and almost certainly also includes contributions from excitation to the $F\,^2\Sigma_g^+$ (and perhaps $G\,^2\Pi_u$) state correlating with the $N^+(^1D) + N(^4S)$ dissociation asymptote [45,49,59,60]. Again, Van Brunt and Kieffer [45,59] have tentatively observed reasonably strong forward-backward scattering anisotropy near threshold over this manifold, consistent with the excitation of states reached via parallel transitions. Angularly resolved photoelectron-photoion coincidence (PEPICO) measurements also support this assignment [61].

Manifold S5 comprises the largest component of the fragment KER distribution for incident electron energies greater than 70 eV, consistent with the retarding potential measurements of Locht *et al.* [46]. This manifold is assigned to the $N^+(^1D) + N(^2D)$ dissociation asymptote. Again, angularly resolved PEPICO measurements indicate strong forward-backward dissociation of the fragment ions over this KER window, indicating significant $^2\Sigma_g^+$ character for the parent state [61].

The contribution to the KER distribution from manifold S6 is reasonably broad, with a tail extending out to ∼6 eV, consistent with sampling of one or more highly repulsive potential curves. This manifold is assigned to the $N^+(^1D) + N(^2P)$ dissociation asymptote.

Considering the above relative contributions and asymptote assignments from each of the single-ionization manifolds, at the lowest electron energy of 30 eV, electron ionization

produces the $N^+(^3P)$ and $N^+(^1D)$ species with ∼80% and ∼20% abundance, respectively. These abundances level out to ∼52% and ∼48% at an electron energy of 100 eV. If the contributions from double ionization (detailed below) are included, electron ionization with 100 eV electrons produces these two atomic ion states in ∼78% and ∼22% abundance, respectively. For comparison, Brenton and co-workers [63] have estimated from $N^+ + O_2$ scattering experiments following production of N^+ using 100 eV electron ionization that ∼86% of N^+ is produced as $N^+(^3P)$ and ∼14% is formed as $N^+(^1D)$. To date, all evidence indicates that $N^+(^1S)$ is a very minor product [12,62].

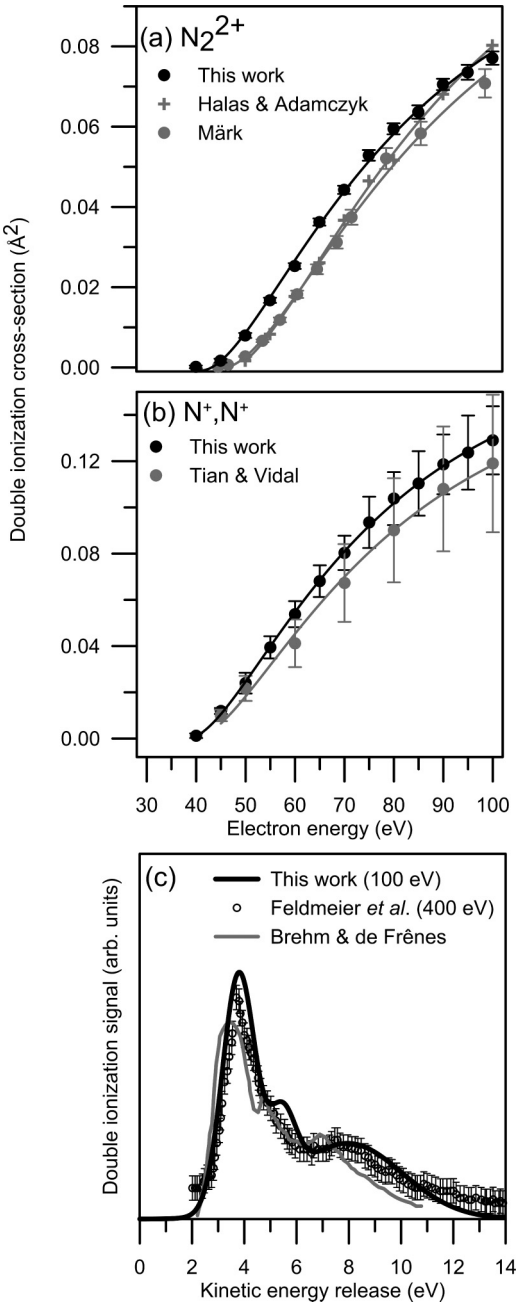

FIG. 3. Comparisons of N_2 double-ionization cross sections with other literature measurements: Märk [65,66], Hałas and Adamczyk [67], Tian and Videl [68], Feldmeier *et al.* [69], and Brehm and de Frênes [70]. The distribution from this work given in (c) is the reconstructed distribution (not crushed).

The doubly charged N_2^{2+} species (D1) is observed as a parentlike feature in the $m/z = 14$ KER distribution, and has a number of long-lived excited states with lifetimes on the time scale of the present measurements [63,64]. The N_2^{2+} counting cross section extracted from the present data (labeled D1 in Fig. 1) is shown in Fig. 3(a), and can be compared with the $^{14}N^{15}N$ measurements of Märk [65], which have been increased by 20% following the discussion in Itikawa [66] and Bull *et al.* [20]. Also included for comparison are the $^{14}N^{15}N$ measurements of Hałas and Adamczyk [67], although these have been renormalized to the gross $m/z = 14$ partial ionization cross section determined in this work because their PICS and total ionization cross section (TICS) in poor agreement with those now well established. Subject to these caveats, there is good overall agreement between the three sets of measurements. The total N^+,N^+ double-ionization (counting) cross section is shown in Fig. 3(b), and is in very good agreement with the heteroisotopic coincidence determination of Tian and Vidal [68]. The total N^+,N^+ double-ionization KER distribution is illustrated in Fig. 3(c), and compares favorably with those from several of the literature coincidence studies [69,70]. Further details of double-ionization cross sections D2, D3, and D4, given in Fig. 2, are discussed in detail in the Supplemental Material [44]. That the present procedure of extracting double-ionization cross sections can reproduce other independent literature measurements on heteroisotopic isotopomers provides confidence that the method provides reliable characterization of the mesoscopic single-ionization channels.

B. Oxygen

Radial distributions of the measured velocity-map images for $m/z = 16$ (transformed into dimensions of KER), together with the forward-convoluted contribution from each basis function, are shown in Fig. 4 for three selected electron

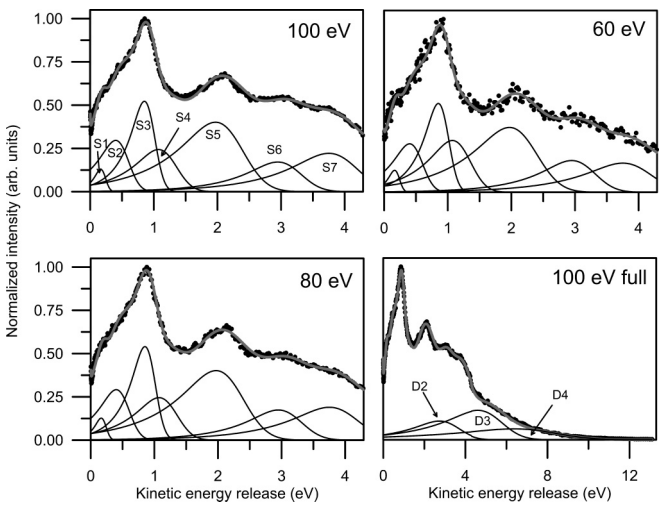

FIG. 4. Radial distributions and final forward-convoluted fits for the images of O^+ and O_2^{2+} formed in the electron ionization of O_2. The O_2^{2+} (D1) contribution is detailed later, and can just be seen in the top left plot near zero KER. Note that the intensity scale is multiplied by the radius in order to better illustrate the high-KER features. S1–S7 and D2–D4 are defined in the text. An example 100 eV velocity-map image is given in the Supplemental Material [44].

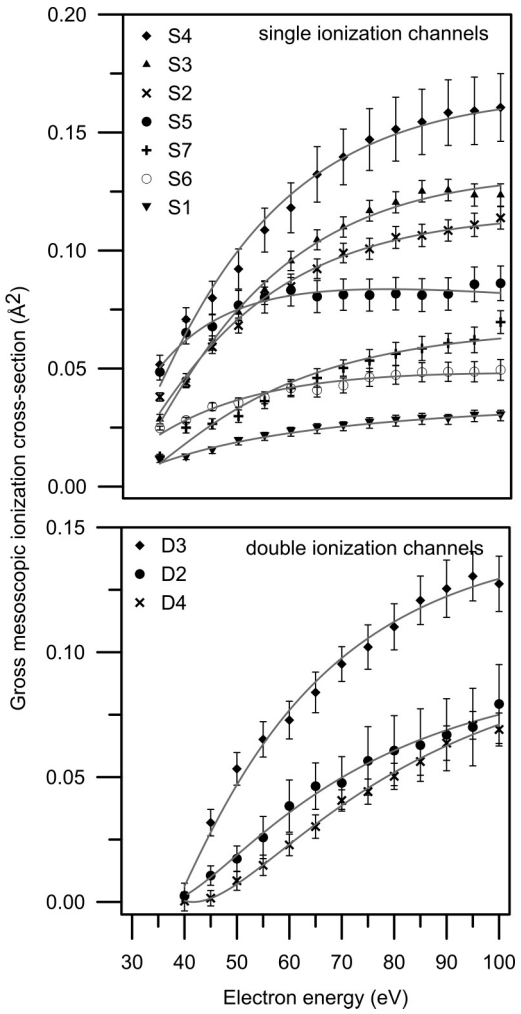

FIG. 5. Mesoscopic ionization cross sections for the ten fragment kinetic-energy release distributions of O^+.

energies. The overall KER distributions are generally in good agreement with a number of previously reported non-imaging measurements, although the earlier measurements suffered ion discrimination effects [39,71]. The 11 basis functions required to achieve a globally acceptable fit have been assigned to seven single-ionization manifolds, denoted S1 to S7, and four double-ionization manifolds, denoted D1 to D4. The mesoscopic cross sections are given in Fig. 5. The mean KERs for the single-ionization contributions are S1 = 0.23(1), S2 = 0.57(1), S3 = 0.99(1), S4 = 1.30(3), S5 = 2.32(4), S6 = 3.24(8), and S7 = 4.1(1) eV. As for N_2, all images have been normalized to the PICS from this instrument and, in turn, the TICS measured as part of this study using the instrument recently detailed in Bull *et al.* [72]. These PICS and TICS are given in the Supplemental Material [44], and are in excellent agreement with the deflection measurements of Straub *et al.* [73] and mass spectrometry measurements of Krishnakumar and Srivastava [74], which have been recommended as literature references in the reviews of Itikawa *et al.* [75,76], Lindsay and Mangan [77], and Raju [78]. An advantage of the present VMI measurement is a high degree of confidence in the measured relative PICSs due to the fact that imaging can ensure that all ions produced with high KER are collected.

As in the case of N_2, manifold S1 is assigned to autoionization of Rydberg states. Mason and Newell [79] and Borst and Zipf [80] performed electron dissociative excitation experiments to characterize KER manifolds predominantly associated with the $O(^5S)$ species near 0.13, and 0.3 eV, respectively. More recently, Matsuo *et al.* [81] have assigned an ionization manifold centered at 0.2 eV to autoionization of Rydberg states converging to the $3\,^2\Pi_u$ state of O_2^+ and correlating with the $O(^1D) + O^+(^4S)$ dissociation asymptote. Other vibrational progression measurements using synchrotron and tunable VUV light sources are in agreement with this assignment [82–85].

Manifolds S2 to S7 correspond to groups of states dissociating to different dissociation asymptotes [39,71]. Potential-energy curves for many low-lying O_2^+ electronic states are given in Lafosse *et al.* [86], and the assignments that follow are consistent with those presented in data from a number of photoionization studies [87–89]. Assuming single-electron ionization of O_2, manifolds S2 to S7 are assigned to the following dissociation asymptotes: S2 corresponds to $O^+(^4S) + O(^3P)$; S3 to $O^+(^4S) + O(^1D)$; S4 to $O^+(^2D) + O(^3P)$; S5 to $O^+(^4S) + O(^1S)$; S6 to $O^+(^2P) + O(^3P)$; and S7 to $O^+(^2D) + O(^1D)$. Rydberg studies indicate that some small proportion of the signal assigned to both S5 and the double-ionization manifolds discussed later results from autoionization processes [71,90].

Manifolds S2 and S3 are thought to arise from both direct dissociation and predissociation of the $B\,^2\Sigma_g^-$ state of O_2^+ [87,91]. Synchrotron studies investigating the competition between the $B\,^2\Sigma_g^-$ state (pre)dissociating to the S2 and S3/S4 asymptotes have found the ratio to be heavily dependent upon the initial vibrational state accessed in the excitation step [92].

Manifold S4 makes the largest contribution to the measured KER distributions; however, the signal from S4 overlaps considerably with that from S3, and the two contributions are therefore not well resolved. Manifolds S5, S6, and S7 have smaller cross sections due to the fact that population of the corresponding states is statistically less probable; electron-impact excitation is generally a relatively inefficient process, and therefore does not efficiently populate the higher-energy states correlating with these dissociation asymptotes. S5 and S6 are thought to arise primarily from the $C\,^4\Sigma_u^-$ and $(3)\,^2\Pi_u$ states, respectively. These two states have been observed to yield O^+ with anisotropic angular distributions in PEPICO measurements [87]. However, the lack of any observable anisotropic dissociation behavior in electron ionization experiments, even in earlier studies with rotatable detectors assuming electron kinetic energies near thresholds, means that confidently assigning each manifold with particular state contributions is not possible.

Based on the above asymptote assignments, around 33% of the signal arising from single ionization of O_2 results from production of electronically excited O^+ ions. Specifically, ~68% of O^+ fragments are formed in the ^4S ground state, ~25% in the ^2D state, and ~8% in the ^2P state, at an incident electron energy of 100 eV. Including contributions from double ionization (detailed below), these percentages

remain approximately the same at ∼69%, ∼25%, and ∼5%, respectively. For comparison, Brenton and co-workers [62,93] have estimated from $O^+ + O_2$ scattering experiments, following 100 eV electron ionization, the total O^+ ionization contributions to be ∼63%, ∼19%, and ∼18%, respectively. Finally, it is noted that a method of characterizing metastable ions from electron ionization has been reported very recently, supporting a small yield of $O^+(^2P)$ from O_2 [94].

Manifold D1 (appearing at very low KER in Fig. 4) corresponds to formation of O_2^{2+} and, similar to N_2^{2+}, the velocity distribution of these ions simply reflects the velocity distribution of the neutral O_2 in the molecular beam. The partial ionization (counting) cross section for production of O_2^{2+} is shown in Fig. 6, along with two other literature measurements for comparison. As was the case for N_2^{2+}, discussed earlier, the heteronuclear $^{17}O^{16}O^{2+}$ data of Märk [65] has been increased by 20% (still assuming Märk's original experimental uncertainties of ±10%) [20,65,75], and at incident electron energies of 80 eV, 94.5 eV, and 100 eV agree within experimental error with those determined in the present work. Also included for comparison is the recent study of Sigaud *et al.* [95], which employed delayed extraction time-of-flight mass spectrometry combined with arrival-time distribution (ATD) fitting in an attempt to extract the O_2^{2+} cross section. Unlike the data recorded in the current study, Sigaud's ATDs are essentially featureless, making it very difficult to extract any physically meaningful contributions from different ion formation pathways from their data. The fitting procedure used in Sigaud's work employed only three Gaussian functions to describe the O^+ ATD, with any near-zero KER O^+ (e.g., autoionization) being subsumed into one or more of these basis functions.

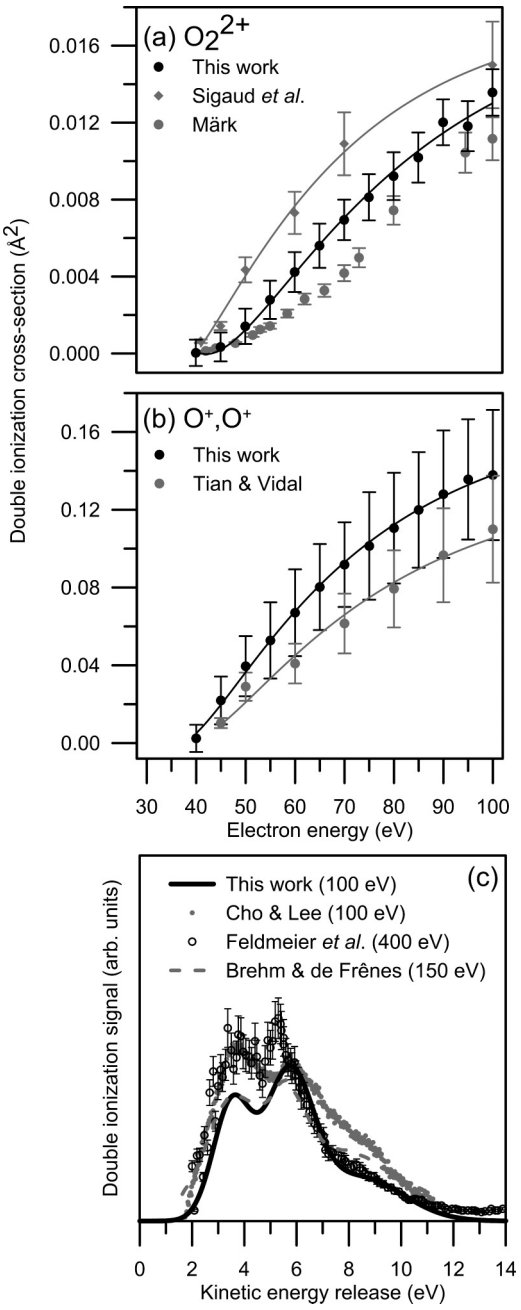

FIG. 6. Comparisons of O_2 double-ionization cross sections with other literature measurements: Märk [65,75], Sigaud *et al.* [95], Tian and Videl [68], Cho and Lee [98], Feldmeier *et al.* [69], and Brehm and de Frênes [70]. Note that the intensities in each curve are arbitrarily scaled so that the spectral features between curves can be compared.

Further, unlike N_2^{2+} above, O_2^{2+} is considerably less stable in the Franck-Condon window due to its lower bond order [96]. Many excited states are metastable with lifetimes on the time scale of nanoseconds to microseconds [96,97]; and predissociation processes contribute significantly to the O^+,O^+ coincidence spectrum. The short O_2^{2+} lifetimes mean that the time scale over which an experiment is performed can have a significant bearing on the ions observed. In the present work, formation, extraction, and detection of O_2^{2+} all occur around 1–2 μs, while Sigaud *et al.* [95] used a pulse sequence such that only dications surviving for over 20 μs could be detected. The timing differences in the two experiments should result in slightly larger measured cross sections for O_2^{2+} in the present work. However, Fig. 6(a) indicates that the cross sections measured by Sigaud *et al.* [95] are systematically larger than those measured in the present work, and do not agree within experimental error. At present, we do not have a comprehensive explanation for this discrepancy.

The total O^+,O^+ double-ionization (counting) cross section is shown in Fig. 6(b), and is in very good agreement with the heteroisotopic coincidence determination of Tian and Vidal [68]. The total O^+,O^+ double-ionization KER distribution is illustrated in Fig. 6(c), and compares favorably with those from several literature coincidence studies [69,70]. Further details of double-ionization cross sections D2, D3, and D4, given in Fig. 5, are discussed in detail in the Supplemental Material [44].

IV. CONCLUSIONS

This paper has presented the results of a velocity-map imaging study into the electron ionization of N_2 and O_2 molecules at electron collision energies between 35 and 100 eV. The study represents a detailed application of velocity-map imaging to investigating the dynamics of electron ionization. Analysis of the measured fragment kinetic-energy release distributions has allowed mesoscopic cross sections to be characterized, providing insight into the contributions from

dissociation processes leading to different product asymptotes as a function of incident electron energy. Cross sections for double-ionization pathways have been measured previously by other authors, and are in good agreement with the data from the present study. This provides confidence in the mesoscopic single-ionization cross sections extracted from the same data sets. Aside from a degree of net forward anisotropy with respect to the electron beam as a result of momentum transfer, all angular fragmentation distributions appear isotropic over the range of incident electron energies studied.

One overall conclusion from this study is that electron ionization is a useful universal ionization mechanism capable of accessing a broad distribution of dissociative ionization channels, although at the cost of selectivity. Even for a simple diatomic it is difficult to deconvolute semi-microscopic channels from the data due to the large number of states from which dissociation occurs. Further information on the electron ionization dynamics could potentially be available through imaging the velocity distribution of the scattered electron, particularly if this could be achieved in coincidence with the fragment ions, and/or electron energy loss spectroscopy.

Finally, whether or not the ionization dynamics are completely understood, the universal and "hard" nature of electron ionization means that it may prove extremely useful as a universal ionization and detection scheme for use in the "probe" step of pump-probe experiments into a variety of molecular phenomena, including laser-initiated photodissociation processes and photoinduced chemical reactions.

ACKNOWLEDGMENTS

Funding is acknowledged from Marie Curie Initial Training Network 238671 "ICONIC," the EPSRC Programme Grant No. EP/G00224X/1, and ERC Starting Independent Research Grant ImageMS. The first two sources provided support from postdoctoral fellowships for J.N.B. while at Oxford, and the second provided financial support for J.W.L.L.

[1] T. D. Märk, *Electron Impact Ionization*, edited by G. H. Dunn (Springer Verlag, Berlin, 1985).
[2] P. Lavvas, M. Galand, R. V. Yelle, A. N. Heays, B. R. Lewis, G. R. Lewis, and A. J. Coates, Icarus **213**, 233 (2011).
[3] D. K. Böhme, Phys. Chem. Chem. Phys. **13**, 18253 (2011).
[4] L. Campbell and M. J. Brunger, Plasma Sources Sci. Technol. **22**, 013002 (2013).
[5] J. L. Fox and G. A. Victor, Planet. Space Sci. **36**, 329 (1988).
[6] R. Thissen, O. Witasse, O. Dutuit, C. S. Wedlund, G. Gronoff, and J. Lilensten, Phys. Chem. Chem. Phys. **13**, 18264 (2011).
[7] D. F. Strobel and D. R. Shemansky, J. Geophys. Res. **87**, 1361 (1982).
[8] D. L. Huestis, S. W. Bougher, J. L. Fox, M. Galand, R. E. Johnson, J. I. Moses, and J. C. Pickering, Space. Sci. Rev. **139**, 63 (2008).
[9] A. J. Coates, F. J. Crary, G. R. Lewis, D. T. Young, J. H. Waite, Jr., and E. C. Sittler, Jr., Geophys. Res. Lett. **34**, L22103 (2007).
[10] H. B. Niemann, S. K. Atreya, S. J. Bauer, G. R. Carignan, J. E. Demick, R. L. Frost, D. Gautier, J. A. Haberman, D. N. Harpold, D. M. Hunten, G. Israel, J. I. Lunine, W. T. Kasprzak, T. C. Owen, M. Paulkovich, F. Raulin, E. Raaen, and S. H. Way, Nature (London) **438**, 779 (2005).
[11] J. H. Waite, Jr., H. Niemann, R. V. Yelle, W. T. Kasprzak, T. Cravens, J. G. Luhmann, R. L. McNutt, W.-H. Ip, D. Gell, V. De La Haye, I. Müller-Wordag, B. Magee, N. Borggren, S. Ledvina, G. Fletcher, E. Walter, R. Miller, S. Scherer, R. Thorpe, J. Xu, B. Block, and K. Arnett, Science **308**, 982 (2005).
[12] O. Dutuit, N. Carrasco, R. Thissen, V. Vuitton, C. Alcaraz, Pernot, N. Balucani, Casavecchia, A. Canosa, S. Le Picard, J.-C. Loison, Z. Herman, J. Zabka, D. Ascenzi, Tosi, Franceschi, S. D. Price, and Lavvas, Astro. Phys. J. Supp. Ser. **204**, 1 (2013).
[13] J. H. Waite, Jr., D. T. Young, T. E. Cravens, A. J. Coates, F. J. Crary, B. Magee, and J. Westlake, Science **316**, 870 (2007).
[14] T. Owen, Nature (London) **438**, 756 (2005).
[15] M. Zhang, J. D. Richardson, and E. C. Sittler, Jr., J. Geophys. Res. **96**, 19085 (1991).
[16] B. A. Smith, L. Soderblom, D. Banfield, C. Barnet, A. T. Basilevsky, R. F. Beebe, K. Bollinger, J. M. Boyce, A. Brahic, G. A. Briggs, R. H. Brown, C. Chyba, S. A. Collins, T. Colvin, A. F. Cook, III, D. Crisp, S. K. Croft, D. Cruikshank, J. N. Cuzzi, G. E. Danielson, M. E. Davies, E. D. Jong, L. Dones, D. Godfrey, J. Goguen, I. Grenier, V. R. Haemmerle, H. Hammel, C. J. Hansen, C. Helfenstein, C. Howell, G. E. Hunt, A. Ingersoll, T. V. Johnson, J. Kargel, R. Kirk, D. I. Kuehn, S. Limaye, H. Masursky, A. McEwen, D. Morrison, T. Owen, W. Owen, J. B. Pollack, C. C. Porco, K. Rages, Rogers, D. Rudy, C. Sagan, J. Schwartz, E. M. Shoemaker, M. Showalter, B. Sicardy, D. Simonelli, J. Spencer, L. A. Sromovsky, C. Stoker, R. G. Strom, V. E. Suomi, S. Synott, R. J. Terrile, Thomas, W. R. Thompson, A. Verbiscer, and J. Veverka, Science **246**, 1422 (1989).
[17] Y. L. Yung and J. R. Lyons, Geophys. Res. Lett. **17**, 1717 (1990).
[18] H. Bethe, Ann. Phys. **5**, 325 (1930).
[19] U. Fano, Phys. Rev. **95**, 1198 (1954).
[20] J. N. Bull, J. W. L. Lee, and C. Vallance, Phys. Chem. Chem. Phys. **15**, 13796 (2013).
[21] D. W. Chandler and P. L. Houston, J. Chem. Phys. **87**, 1445 (1987).
[22] A. T. J. B. Eppink and D. H. Parker, Rev. Sci. Instrum. **68**, 3477 (1997).
[23] D. H. Parker and A. T. J. B. Eppink, J. Chem. Phys. **107**, 2357 (1997).
[24] *Imaging in Molecular Dynamics*, edited by B. J. Whitaker (Cambridge University Press, New York, 2003).
[25] M. N. R. Ashfold, N. H. Nahler, A. J. Orr-Ewing, O. J. Vieuxmaire, R. L. Toomes, T. N. Kitsopolulos, I. A. Garcia, D. A. Chestakov, S.-M. Wu, and D. H. Parker, Phys. Chem. Chem. Phys. **8**, 26 (2006).
[26] A. I. Chichinin, K. H. Gericke, S. Kauczok, and C. Maul, Int. Rev. Phys. Chem. **28**, 607 (2009).
[27] S. J. Greaves, R. A. Rose, and A. J. Orr-Ewing, Phys. Chem. Chem. Phys. **12**, 9129 (2010).
[28] P. W. Harland, B. R. Cameron, M. Bart, and M. O. Pearce, Rev. Sci. Instrum. **73**, 2398 (2002).
[29] B. Wu, L. Xia, H.-K. Li, X.-J. Zeng, and S. X. Tian, Rev. Sci. Instrum. **83**, 013108 (2012).

[30] B.-Y. Chang, R. C. Hoetzlein, J. A. Mueller, J. D. Geiser, and L. Houston, Rev. Sci. Instrum. **69**, 1665 (1998).
[31] K. Stephan, H. Helm, and T. D. Märk, J. Chem. Phys. **73**, 3763 (1980).
[32] A. Kobayashi, G. Fukjiki, A. Okaji, and T. Masuoka, J. Phys. B: At. Mol. Opt. Phys. **35**, 2087 (2002).
[33] G. H. Dunn., Phys. Rev. Lett. **8**, 62 (1962).
[34] G. H. Dunn and L. J. Kieffer, Phys. Rev. **132**, 2109 (1963).
[35] R. N. Zare, J. Chem. Phys. **47**, 204 (1967).
[36] M. Misakian, J. C. Pearl, and M. J. Mumma, J. Chem. Phys. **57**, 1891 (1972).
[37] R. J. Van Brunt and L. J. Kieffer, Phys. Rev. A **2**, 1293 (1970).
[38] R. J. Van Brunt, J. Chem. Phys. **60**, 3064 (1974).
[39] J. A. D. Stockdale and L. Deleanu, Chem. Phys. Lett. **22**, 204 (1973).
[40] C. G. Aitken, D. A. Blunt, and W. Harland, J. Chem. Phys. **101**, 11074 (1994).
[41] C. G. Aitken, D. A. Blunt, and W. Harland, Int. J. Mass Spectrom. Ion Proc. **149-150**, 279 (1995).
[42] G. M. Roberts, J. L. Nixon, J. Lecoitre, E. Wrede, and J. R. R. Verlet, Rev. Sci. Instrum. **80**, 053104 (2009).
[43] E. U. Condon, Phys. Rev. **32**, 858 (1928).
[44] See Supplemental Material at http://link.aps.org/supplemental/10.1103/PhysRevA.91.022704 for O_2 partial ionization cross sections, an example velocity-map image, description of double-ionization channels, and tabulation of all cross sections determined in this study.
[45] R. J. Van Brunt and L. J. Kieffer, J. Chem. Phys. **63**, 3216 (1975).
[46] R. Locht, J. Schopman, H. Wankenne, and J. Momigny, Chem. Phys. **7**, 393 (1975).
[47] L. Deleanu and J. A. D. Stockdale, J. Chem. Phys. **63**, 3898 (1975).
[48] K. Köllmann, Int. J. Mass Spectrom. Ion Phys. **17**, 261 (1975).
[49] T. Aoto, K. Ito, Y. Hikosaka, A. Shibasaki, R. Hirayama, N. Yamamono, and E. Miyoshi, J. Chem. Phys. **124**, 234306 (2006).
[50] A. Crowe and J. W. McConkey, J. Phys. B: At. Mol. Opt. Phys. **6**, 2108 (1973).
[51] K. C. Smyth, J. A. Schiavone, and R. S. Freund, J. Chem. Phys. **59**, 5225 (1973).
[52] W. C. Wells, W. L. Borst, and E. C. Zipf, Phys. Rev. A **14**, 695 (1976).
[53] S. Oshima, T. Kondow, T. Fukuyama, and K. Kuchitsu, Chem. Phys. **85**, 403 (1984).
[54] T. Ogawa, S. Ishibashi, J. Kurawaki, and H. Kawazumi, J. Chem. Phys. **82**, 1920 (1985).
[55] C. Nicolas, C. Alcaraz, R. Thissen, M. Vervloet, and O. Dutuit, J. Phys. B.: At. Mol. Opt. Phys. **36**, 2239 (2003).
[56] Y. Morioka, T. Akahori, T. Hayaishi, T. Namioka, T. Sasaki, and M. Nakamura, J. Phys. B: At. Mol. Opt. Phys. **19**, 1075 (1986).
[57] Y. Morioka, S. Aoyama, Y. Kageyama, T. Hayaishi, I. H. Suzuki, G. Isoyama, S. Asaoka, E. Ishiguro, and M. Nakamura, J. Phys. B.: At. Mol. Opt. Phys. **17**, 2795 (1984).
[58] A. L. Roche and J. Tellinghuisen, Mol. Phys. **38**, 129 (1979).
[59] L. J. Kieffer and R. J. Van Brunt, J. Chem. Phys. **46**, 2728 (1967).
[60] M. Lucchini, K. Kim, F. Calegari, F. Kelkensberg, W. Siu, G. Sansone, M. J. J. Vrakking, M. Hochlaf, and M. Nisoli, Phys. Rev. A **86**, 043404 (2012).
[61] J. H. D. Eland and E. J. Duerr, Chem. Phys. **229**, 13 (1998).
[62] A. R. Lee, C. S. Enos, and A. G. Brenton, Chem. Phys. **150**, 275 (1991).
[63] F. R. Bennett, J. Chem. Phys. **103**, 3613 (1995).
[64] D. Mathur, L. H. Andersen, Hvelplund, D. Kella, and C. Safvan, J. Phys. B: At. Mol. Opt. Phys. **28**, 3415 (1995).
[65] T. D. Märk, J. Chem. Phys. **63**, 3731 (1975).
[66] Y. Itikawa, J. Phys. Chem. Ref. Data **35**, 31 (2006).
[67] S. Hałas and B. Adamczyk, Int. J. Mass Spectrom. Ion Phys. **10**, 157 (1972).
[68] C. Tian and C. R. Vidal, J. Phys. B: At. Mol. Opt. Phys. **31**, 5369 (1998).
[69] F. Feldmeier, H. Durchholz, and A. Hofmann, J. Chem. Phys. **79**, 3789 (1983).
[70] B. Brehm and G. de Frênes, Int. J. Mass Spectrom. Ion Phys. **26**, 251 (1978).
[71] R. J. Van Brunt, G. M. Lawrence, L. J. Kieffer, and J. M. Slater, J. Chem. Phys. **61**, 2032 (1974).
[72] J. N. Bull, J. W. L. Lee, and C. Vallance, Phys. Chem. Chem. Phys. **16**, 10743 (2014).
[73] H. C. Straub, P. Renault, B. G. Lindsay, K. A. Smith, and R. F. Stebbings, Phys. Rev. A **54**, 2146 (1996).
[74] E. Krishnakumar and S. K. Srivastava, Int. J. Mass Spectrom. Ion Proc. **113**, 1 (1992).
[75] Y. Itikawa, A. Ichimura, K. Onda, K. Sakimoto, K. Takayanagi, Y. Hatano, M. Hayashi, H. Nishimura, and S. Tsurubuchi, J. Phys. Chem. Ref. Data **18**, 23 (1989).
[76] Y. Itikawa, J. Phys. Chem. Ref. Data **38**, 1 (2009).
[77] B. G. Lindsay and M. A. Mangan, *Photon- and Electron-Interactions with Molecules: Ionization and Dissociation*, edited by Y. Itikawa (Springer, New York, 2003), Chap. 5.
[78] G. G. Raju, *Gaseous Electronics: Tables, Atoms, and Molecules* (CRC, Boca Raton, FL, 2012).
[79] N. J. Mason and W. R. Newell, J. Phys. B: At. Mol. Opt. Phys. **23**, 4641 (1990).
[80] W. L. Borst and E. C. Zipf, Phys. Rev. A **4**, 153 (1971).
[81] A. Matsuo, K. Furuya, and T. Ogawa, Chem. Phys. Lett. **287**, 653 (1998).
[82] Y. Lu, Z. X. He, J. N. Cutler, S. H. Southworth, W. C. Stole, and J. A. R. Samson, J. Elec. Spectrosc. Rel. Phenom. **94**, 135 (1998).
[83] B. L. G. Bakker, D. H. Parker, C. Samartzis, and T. N. Kitsopoulos, J. Chem. Phys. **112**, 5654 (2000).
[84] P. Erman, A. Karawajczyk, E. Rachlew-Källne, M. Stankiewicz, and K. Y. Franzén, J. Phys. B.: At. Mol. Opt. Phys. **29**, 5785 (1996).
[85] A. A. Wills, A. A. Cafolla, and J. Comer, J. Phys. B.: At. Mol. Opt. Phys. **24**, 3989 (1991).
[86] A. Lafosse, J. C. Brenot, A. V. Golovin, M. Guyon, K. Hoejrup, J. C. Houver, M. Lebech, and D. Dowek, J. Chem. Phys. **114**, 6605 (2001).
[87] J. H. D. Eland and E. J. Duerr, Chem. Phys. **229**, 1 (1998).
[88] K. Ellis, R. I. Hall, L. Avaldi, G. Dawber, A. McConkey, L. Andrić, and G. C. King, J. Phys. B.: At. Mol. Opt. Phys. **27**, 3415 (1994).
[89] J. L. Gardner and J. A. R. Samson, J. Chem. Phys. **62**, 4460 (1975).
[90] R. S. Freund, J. Chem. Phys. **54**, 3125 (1971).
[91] C. J. Danby and J. H. D. Eland, Int. J. Mass Spectrom. Ion Phys. **8**, 153 (1972).

[92] X. Tang, X. Zhou, M. Niu, S. Liu, and L. Sheng, J. Phys. Chem. A **115**, 6339 (2011).
[93] M. Hamdan and A. G. Brenton, J. Phys. B: At. Mol. Opt. Phys. **22**, 2289 (1989).
[94] J. J. Corr, M. A. Kahkoo, A. G. McConkey, and J. W. McConkey, Int. J. Mass Spectrom. **376**, 19 (2015).
[95] L. Sigaud, N. Ferreira, and E. C. Montenegro, J. Chem. Phys. **139**, 024302 (2013).
[96] D. Edvardsson, S. Lunell, F. Rakowitz, C. M. Marian, and L. Karlsson, Chem. Phys. **229**, 203 (1998).
[97] M. Lundqvist, D. Edvardsson, Baltzer, M. Larrson, and B. Wannberg, J. Phys. B: At. Mol. Opt. Phys. **29**, 499 (1996).
[98] H. Cho and S. H. Lee, Phys. Rev. A **48**, 2468 (1993).